SAE INTERNATIONAL®

Effects of In-Cylinder Mixing on Low Octane Gasoline Compression Ignition Combustion	2016-01-0762
	Published 04/05/2016

Jihad Badra
Saudi Aramco

Ahmed Elwardany and Jaeheon Sim
King Abdullah University of Science and Technology

Yoann Viollet
Saudi Aramco

Hong Im
King Abdullah University of Science and Technology

Junseok Chang
Saudi Aramco

Abstract

Gasoline compression ignition (GCI) engines have been considered an attractive alternative to traditional spark ignition engines. Low octane gasoline fuel has been identified as a viable option for the GCI engine applications due to its longer ignition delay characteristics compared to diesel and in the volatility range of gasoline fuels. In this study, we have investigated the effect of different injection timings at part-load conditions using light naphtha stream in single cylinder engine experiments in the GCI combustion mode with injection pressure of 130 bar. A toluene primary reference fuel (TPRF) was used as a surrogate for the light naphtha in the engine simulations performed here. A physical surrogate based on the evaporation characteristics of the light naphtha has been developed and its properties have been implemented in the engine simulations. Full cycle GCI computational fluid dynamics (CFD) engine simulations have been successfully performed while changing the start of injection (SOI) timing from -50° to -11 ° CAD aTDC. The effect of SOI on mixing and combustion phasing was investigated using detailed equivalence ratio-temperature maps and ignition delay times. Both experimental and computational results consistently showed that an SOI of -30° CAD aTDC has the most advanced combustion phasing (CA50), with the highest NOx emission. The effects of the SOI on the fuel containment in the bowl of the piston, the ignition delay time, combustion rate and emissions have been carefully examined through the CFD calculations. It was found that the competition between the equivalence ratio and temperature is the controlling parameter in determining the combustion phasings.

Introduction

The demand on global transport energy is expected to increase by around 40% by 2040 [1, 2, 3, 4]. This large increase in demand will primarily be in non-organization for economic co-operation and development (OECD) countries. More than 90% of the global transport energy demand is supplied by the petroleum-based liquid fuels such as gasoline, diesel, jet and heavy fuel oil fuels [2]. Therefore, improving the fuel efficiency at low cost in transportation sector can help not only saving the global energy usage but also reducing the greenhouse gas (GHG) CO_2 emissions.

Gasoline and diesel engines have been around for a long time and lots of research has been focusing on enhancing the efficiency and reducing the harmful emissions from these engines. Gasoline compression ignition (GCI) is emerging as a new technology and attracting increased attention. One of the advantages that GCI engines have is that they can operate at low temperature combustion (LTC) conditions. This combustion mode has been gaining increasing attention over the last decade due to its potential of achieving diesel-like thermal efficiencies with significantly reduced engine-out nitrogen oxides (NOx) and soot emissions. Recent studies [5, 6, 7, 8, 9, 10, 11, 12, 13, 14, 15, 16, 17, 18] reported that GCI combustion occurs as a series of autoignition events with minor contributions from the flame fronts. This is usually achieved by controlling the autoignition timing by manipulating equivalence ratio stratification levels within the cylinder through late injection in the compression stroke, in contrast to homogeneous charge compression ignition (HCCI) [19, 20, 21, 22] and premixed ignition [23, 24] engines where

the fuel and air are fully mixed prior to entering the combustion chamber. The enabling fuel for such GCI combustion is lesser processed, compared to commercial gasoline and diesel fuels, refinery streams such as, petroleum naphtha with octane numbers (RON) in the 50-80 range. This low octane petroleum naphtha appears to be very attractive solution not only for providing suitable chemical characteristics (longer ignition delay than diesel fuel) for just enough mixing, but also lesser processed than production gasoline fuel and help saving CO_2 emissions from the refinery process (Well-to-Tank GHG emission).

The petroleum naphtha GCI combustion process has not yet been studied thoroughly. It is predominantly premixed combustion, however, the mixing and spray/piston interactions are very important parameters to help understanding and optimizing these engines. Therefore, simulation is a valuable tool that can aid the development and design of advanced GCI combustion modes. Full cycle computational fluid dynamics (CFD) simulations with detailed chemical kinetics and turbulent transport provide fundamental understanding of the spray development and stratification and their effects on the combustion process. Ra et al. [25] performed extensive numerical studies on GCI combustion to investigate the effects of injection parameters, gas temperatures, boost pressure and exhaust gas recirculation (EGR) on combustion characteristics such as combustion phasing and important emissions. As a specific example, they [15] have demonstrated that triple injection GCI helped achieving high load operation through parametric simulations. Recently, Badra et al. [26] reported a numerical study on the optimization of the spray models for outwardly opening hollow cone spray and the effects of primary reference fuel (PRF) and toluene primary reference fuel (TPRF) chemical surrogates on the combustion phasing of GCI engine running on naphtha fuel.

The robustness of the spray breakup, evaporation, mixing and combustion models are very critical for predictive GCI engine simulations. Events such as the distribution and concentration of fuel vapor directly affect the combustion efficiency and emissions [27, 28]. The atomized spray breakup enhances fuel evaporation and combustion rate. In the past, the inwardly opening pressure swirl hollow cone spray injector has been commonly used due to its efficient atomization with wide spray angle and fine atomization characteristics [29]. Recently, the outwardly opening piezo-injector has been gaining popularity in favor of its higher efficiency and easier control of the spray flow [30].

In this work, experimental data that investigated the effect of injection timings on the combustion phasing and emissions formation in GCI engine running on petroleum naphtha were reported. A methodology to model the outwardly opening hollow cone injector was developed using 3D CFD simulations. Furthermore, the heating and evaporation of a single droplet were modeled in order to determine the heating and evaporative characteristics of the real light naphtha fuel and its TPRF and multi-component surrogates. Finally, full-cycle GCI engine 3D CFD simulations were performed and compared with experimental data. The in-cylinder fuel air mixing has been thoroughly investigated through detailed reacting and non-reacting equivalence ratio-temperature (Φ-T) maps and homogeneous ignition delay times.

Experimental Setup

Engine Combustion Chamber Configuration

A single cylinder 4 valve engine with a 14:1 geometric compression ratio is used in this investigation. Table 1 shows the details of the engine specifications. The combustion chamber is originally designed to accommodate stratified charge spark ignition combustion. An outwardly opening piezo-electric hollow cone GDI injector is centrally mounted adjacent to the spark plug. In GCI combustion tests, the spark is disabled. As seen in Figure 1, the injector is located between two intake valves and slightly skewed from the vertical direction. Fuel is introduced by an outwardly opening piezo-electric injector with hollow cone spray. The spray is more widely distributed with less penetration compared to spray-jet style multi-hole type gasoline direct injector. The operating fuel injection pressure range is 50-150 bars, which is about 10 times lower than a conventional diesel injector. As such, spray atomization and penetration characteristics are expected to be significantly different.

For the purpose of this study, a new set of pistons was designed and manufactured. To improve fuel containment, a diesel bowl-like feature was added. It also has a reentry feature to ensure that spray interaction occurs inside the bowl. The squish height is 1.5mm (yellow). Since the combustion chamber is originally made for a gasoline engine (pent-roof style), the piston height is relatively large in order to match the CR and compensate the bowl volume, resulting in a smaller clearance height than a conventional gasoline piston. As seen in Figure 2 (side view), the spark plug is still installed although it was not utilized in this study. The crevice in the spark plug can be considered as a major source of HC emissions if fuel spray is steered near the spark plug.

Table 1. Single cylinder engine specifications.

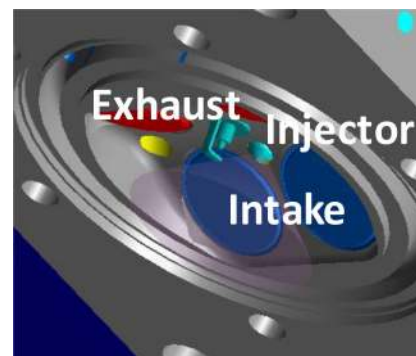| Cylinders	1
Number of Valves	4
Displacement	499 cc
Bore	84 mm
Stroke	90 mm
Connecting Rod	159 mm
Compression ratio	14:1
Swirl Ratio	0
Fuel Injector	Direct Injector Outwardly Opening Piezo-Electric (GDI) (BMW Siemens)
Fuel Pump Range	40-150bar
Intake System	Conditioned Air with External Boost
Exhaust System	Back pressure valve

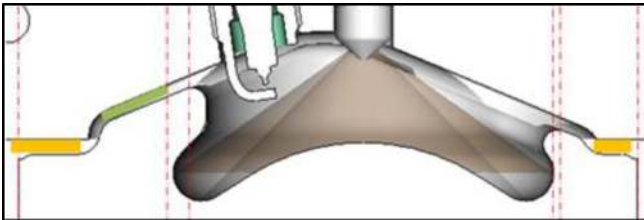Figure 1. Base engine Combustion Chamber Shape: Pent-Roof Style 4 Valve Head.

Figure 2. Side view picture of compression ratio 14 piston: incorporating diesel bowl reentry feature.

Figure 3. Top and full views of the GCI piston CR14.

GCI testing was performed with fixed intake and exhaust valve events and symmetric lift profiles (8 mm peak lift and 207 CAD duration), as shown in Figure 4. This is similar to conventional production diesel valve lift profiles.
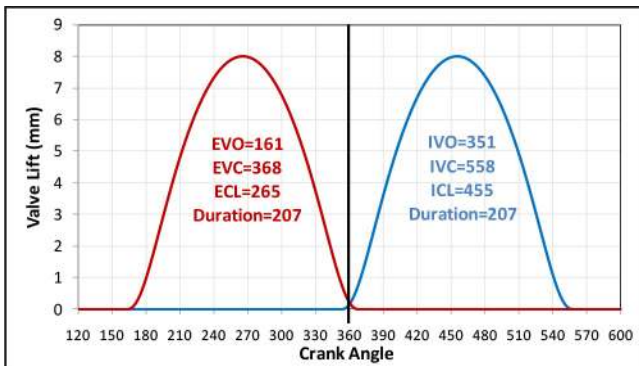

Figure 4. GCI valve lift profile: 8mm peak lift, no variable valve timing with minimum valve overlap.

Data acquisition system

Pressure is measured using the Kistler pressure sensors and charge amplifiers along with a Leine and Linde 500 series crank angle encoder. The sampling resolution was adjusted to 0.3 Crank Angle Degree (CAD). Averaged pressure traces are based on the acquisition of 300 combustion cycles. Experimental indicated mean effective pressure (IMEP), net mean effective pressure (NMEP), pumping mean effective pressure (PMEP), are calculated in real time with FEV CAS (FEV combustion analysis system). Table 2 lists the locations and types of the pressure sensors used for measuring the intake, exhaust and cylinder pressures.

Table 2. Crank angle resolved sensors description.

Measurement	Location	Type
Intake pressure	200 mm back of valve	4045A (piezo resistive)
Cylinder pressure	Flush mounted yellow spot in Figure 1	6061B (quartz water cooled)
Exhaust pressure	160 mm back of valve	4045A (piezo resistive water cooled)

NOx and HC are measured in wet condition. Air fuel ratio is calculated by the Horiba emission bench where lambda is calculated using the Brettschneider/Spindt formula. Smoke emissions are obtained by means of an AVL415S smoke meter and probe inserted into the exhaust gas stream. The exhaust temperature is measured via a K type thermocouple whereas all others temperatures are measured with PT100 thermocouples. Engine coolant and lubricant temperature is maintained at 90°C. Air temperature at the inlet of the intake plenum is adjusted to 25°C without EGR activation and from that point intake manifold air temperature increases gradually as a function of the EGR rate (approx. 30°C with no EGR). A Siemens DI1.5 flow meter relying on the Coriolis principle measures the fuel mass flow supplied to the engine. Airflow measurement is covered by the ABB SensyFlow hotwire mass flow meter.

The fuel used in all the experiments in this work is the straight run Saudi Aramco light naphtha. The light naphtha properties are listed in Table 3.

Table 3. Saudi Aramco light naphtha fuel properties.

Property	Saudi Aramco light naphtha
DCN from IQT	34
RON	68
MON	63
Sensitivity	5
Density (kg/m^3)	656
LHV (MJ/kg)	44.9
H/C ratio	2.266
Normal-paraffins vol%	53.3
Iso-paraffins vol%	39.6
Aromatics vol%	0.9
Naphthenes vol%	6.2
Olefins vol%	0
Oxygenates vol%	0
Sulfur (ppm)	<20

Numerical Setup

Engine and Spray Modeling

CONVERGE [31] is used to perform the CFD simulations in this work. CONVERGE [31] is a general purpose CFD code to solve multi-dimensional reacting flows with stationary and moving boundaries. It contains models for spray, turbulence, liquid drop dynamics and combustion. More detailed descriptions of the models can be found in [31]. The RANS-based turbulent models are used throughout the simulations presented in this work. The SAGE detailed chemistry solver [32] along with multi-zone approach is used as a combustion sub-model. The NOx and soot emissions are enabled using the extended Zel'dovich NOx [33] and Hiroyasu soot [34] models, respectively. Grid generation is done during run-time by utilizing both fixed embedding of cells and adaptive mesh refinement (AMR) based on key parameters gradients.

Regarding the spray modeling, a Lagrangian discrete parcel method is used by introducing parcels (groups of droplets) of liquid into the gas phase computational domain because it is beyond the current computational scope to conduct complete direct numerical simulations of multi-phase interaction between gas and many small spray droplets. The spray from the outwardly opening piezo-injector is considered as a hollow-cone spray with string-like structures at the nozzle exit [35]. However, the mechanism of string-like structure has not yet been understood, and no appropriate models to predict such a string formation and accurate droplet sizes exist in the literature.

In this study, the modified Kelvin-Helmholtz and Rayleigh-Taylor (KH-RT) breakup model is implemented by feeding small cylindrical liquid blobs along the circular liquid sheet of a hollow-cone spray.

The details of nozzle flow and the inside structure of the injector is mostly unknown. However, the steady injection velocity can be estimated by the Bernoulli equation, the density of the liquid (ρ_l) and the nozzle's discharge coefficient (C_D). The injection velocity (U) is dependent on the pressure difference (Δp) between the injection (p_{inj}) and chamber pressure (p_c):

$$U = C_D \sqrt{\frac{2(p_{inj} - p_c)}{\rho_l}}$$

(1)

In the original linear instability sheet atomization (LISA) breakup model for pressure-swirl injectors, a velocity coefficient (k_v) is used instead of discharge coefficient (C_D) in Eq. (1), and a correlation for the coefficient has been suggested [36]. Later, Schmidt et al. [37] estimated the velocity coefficient from a typical value (0.78) of the discharge coefficient of a single nozzle with sharp inlet corners by reducing the value by 10% for extra momentum losses, such that

$$k_v = \max\left[0.7, \frac{4\dot{m}}{\pi d_n^2 \rho_l \cos(\theta)} \sqrt{\frac{\rho_l}{2\Delta p}}\right],$$

(2)

where θ is the half of spray angle and d_n is the nozzle diameter. This velocity coefficient agrees with the definition of the discharge coefficient. Therefore, the nozzle's discharge coefficient (C_D) of 0.7 is used for the injection velocity calculation in the present outwardly opening hollow-cone spray simulations. From Schmidt et al. [37], the initial sheet thickness of the liquid film (t_0) can be obtained from the known mass flow rate ($\dot{m}$) and the injection velocity (U) by

$$\dot{m} = \pi \rho U \cos(\theta) t_0 (d_n - t_0)$$

(3)

The calculated liquid sheet thickness is a starting point in our spray modeling regardless of breakup or collision models. In the present study, modified KH-RT is implemented. For the modified KH-RT breakup model, the initial SMD is the most ambiguous parameter. The initial liquid sheet thickness (t_0) of Eq. (3) can be considered as an initial SMD. However, it does not comply with the liquid jet stability analysis in the Kelvin-Helmholtz instability because the spray is a circular liquid film with a thickness. The experimentally observed string-like structure of hollow-cone spray favors the KH-RT models since the spray is considered many small solid cone injections along a circular liquid sheet. Therefore, the initial SMD of the string-like liquid film is calculated by assuming that the cylindrical liquid blobs are attached to each other:

$$D_{0,string} = \frac{4}{\pi} t_0$$

(4)

For the liquid jet stability analysis to be valid, the cylindrical liquid blobs must be detached from each other, but Eq. (4) serves as a starting point for the implementation of non-LISA breakup models for hollow-cone sprays.

The Rosin-Rammler injection size distribution models are used with a distribution parameter of 3.5 for modified KH-RT breakup model for better accuracy. Furthermore, the dynamic drag model was implemented by determining the droplet drag coefficient dynamically, accounting for variations in the drop shape through a drop distortion parameter for accurate spray modeling. The effect of the turbulent flow on spray drops is modeled using O'Rourke's turbulent dispersion model by accounting a fluctuating velocities [38]. For collision model, the traditional O'Rourke collision scheme [38] and no-time-counter (NTC) method [39] are tested, and extended with Post and Abraham's inclusion of collision regimes [40]. For spray evaporation, Frossling's [41] evaporation model is implemented in this work with all base parcel species are considered as evaporation source.

The complete single cylinder engine geometry is meshed and used in the subsequent engine CFD simulations. The engine specifications are presented in Table 1. The base mesh size used in this work is 4 mm. The mesh is refined to 2 mm in a geometrical cylinder that contains the cylinder region and a part of the intake and exhaust ports. The cylinder region has additional embedding levels with the base grid size of 1mm. The mesh in contact with the intake and exhaust valve seats is refined to 0.5mm. The mesh near the nozzle exit is refined to 0.25mm when injection is taking place. In addition to these fixed embedding refinements, temperature and velocity AMR with an embedding level of 3 for each, resulting in the smallest grid size of 0.25 mm in the domain. This proved to produce grid independent solution for the simulated motored runs and hence the same mesh is utilized for the subsequent GCI cases. Kodavasal et al. [18] showed that a finer grid might be needed to reach grid independent solution for reacting cases; however, the current grid is considered sufficient for the objectives of this study which is mainly examining the mixing effect on combustion phasing. The reduced TPRF chemical kinetic models developed by Liu et al. [42] (56 species and 168 reactions) is used in this work.

Droplet Heating and Evaporation Modeling

Accurate modeling of heating and evaporation affects all subsequent processes including mixing and autoignition [43]. The heating and evaporation model is based on the analytical solutions of the heat conduction and species diffusion equations inside a spherical droplet [44] and referred to as effective thermal conductivity/effective diffusivity (ETC/ED) model. The model was originally developed for bi-component droplets heating and evaporation [45] and it was generalized to multi-component fuel droplets for diesel, gasoline and different types of biofuels in [46, 47, 48]. The model accounts for actual fuel composition, finite liquid thermal conductivity, finite species diffusivities and recirculation inside the droplet.

Experimental Results

SOI Sweep

An injection timing sweep was performed at 1500RPM 1.2 bar abs intake pressure and intake temperature of 32°C. No EGR was applied. The engine RPM, NMEP, intake temperature and intake

pressure were kept constant while performing the SOI sweep. Only the injection duration and injected fuel mass were slightly changed to match the NMEP. The experimental conditions for the different tested cases are listed in Table 4. The injection timing varied from -11 to -50 CAD aTDC. The in-cylinder pressure traces from the different test conditions are shown in Figure 5. It is seen that the combustion phasing is advanced most for early injections such as -50, -40 and -30 CAD aTDC. Retarding the injection further than -30 CAD aTDC causes the combustion phasing to be delayed as can be seen from the pressure traces for the -18, -14 and -11 CAD aTDC SOI presented in Figure 5. The HC, CO, NOx and smoke number emissions along with the combustion efficiency and maximum pressure rise are plotted in Figure 6 for different SOI. Figure 6 shows that the minimum HC and CO emissions were reached at -18CAD aTDC timing with 150 ppm of HC and 0.05% of CO. This also matched with the peak of combustion efficiency (calculated based on the emission bench values). NOx emissions reached a peak at -30 CAD aTDC with 715 ppm. This coincided with the region of maximum pressure rise rate measured by the combustion analysis system. However, with further advancement or retardation of the injection timing, NOx dropped rapidly to 100 ppm and 178 ppm at - 50 CAD aTDC and -11 CAD aTDC, respectively. Smoke emission was overall very low and increased with later injection timings as expected because of the lesser time available for mixing and hence the presence of richer pockets that produce more soot.

Table 4. Experimental conditions of the different examined cases with various injection timings.

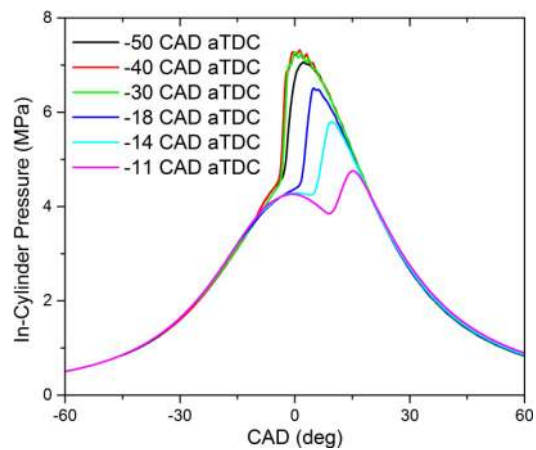| RPM	1500	1500	1500	1500	1500	1500
NMEP (bar)	3.6	3.6	3.6	3.6	3.6	3.6
Intake Temperature (°C)	32	32	32	32	32	32
Intake pressure (bar)	1.2	1.2	1.2	1.2	1.2	1.2
Injection pressure (bar)	130	130	130	130	130	130
SOI (aTDC)	-50	-40	-30	-18	-14	-11
Injection duration (ms)	0.329	0.341	0.358	0.381	0.397	0.418
Injected mass (mg/cycle)	9.556	9.578	9.667	9.267	9.867	9

Figure 5. Experimental in-cylinder pressure from the tested cases described in Table 4.
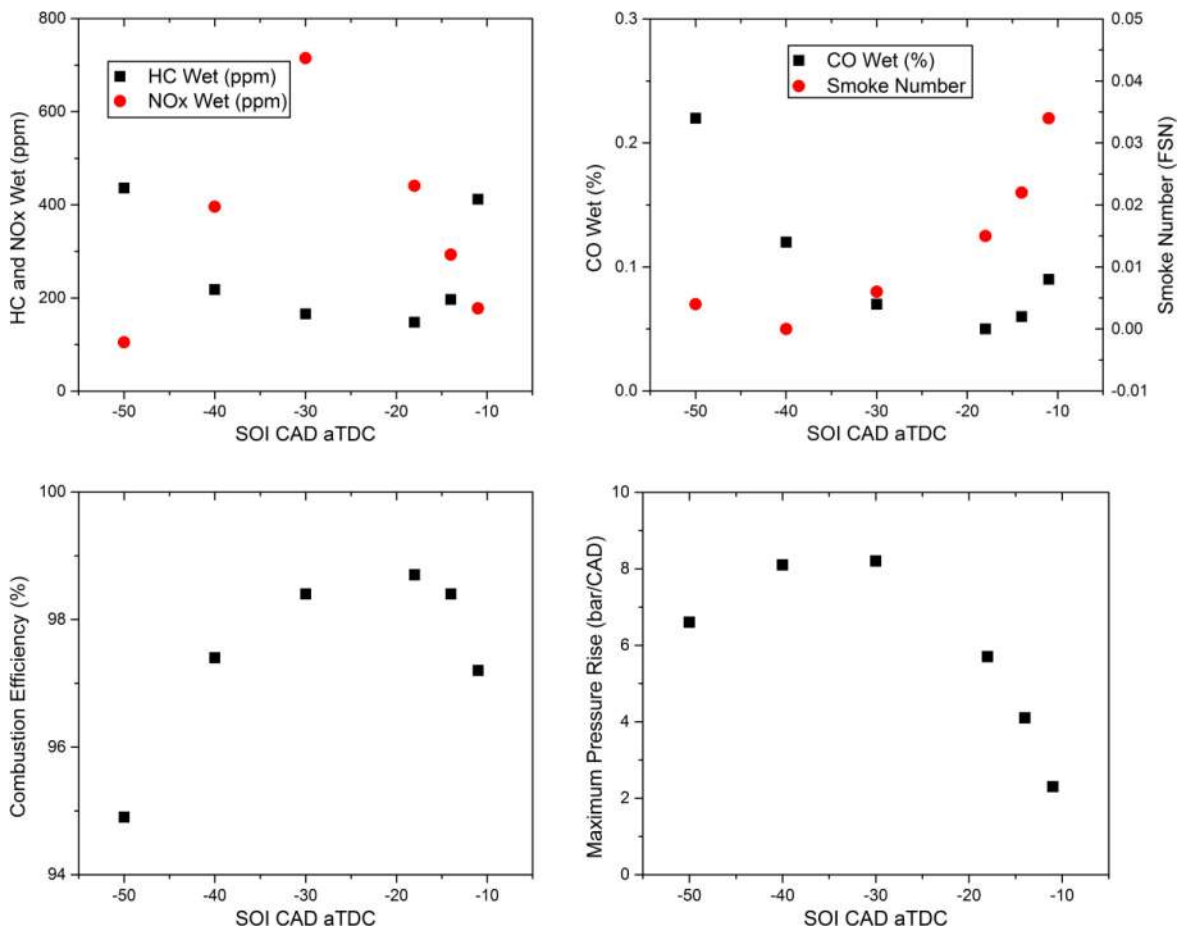

Figure 6. HC, CO, NOx and smoke number emissions along with the combustion efficiency and maximum pressure rise for the tested SOI.

The IMEP COV and the ignition delay defined as CA10-SOI are presented in Figure 7 for the various tested SOI. As can be observed from Figure 7, optimal combustion stability was achieved at -18 CAD aTDC with less than 1% IMEP.COV. Slightly higher values were recorded at the other injection timings but they overall remained very good with values consistently below 3% IMEP.COV. The shortest ignition delay measured was 2.2 ms at both -18 and -14 CAD aTDC. It corresponded to the area of best combustion stability (lowest IMEP.COV). This is an interesting behavior where the combustion is more stable when more stratification is present. Also, the CA10, 50 and 90 are more sensitive to the SOI at these later injections unlike the early SOI.
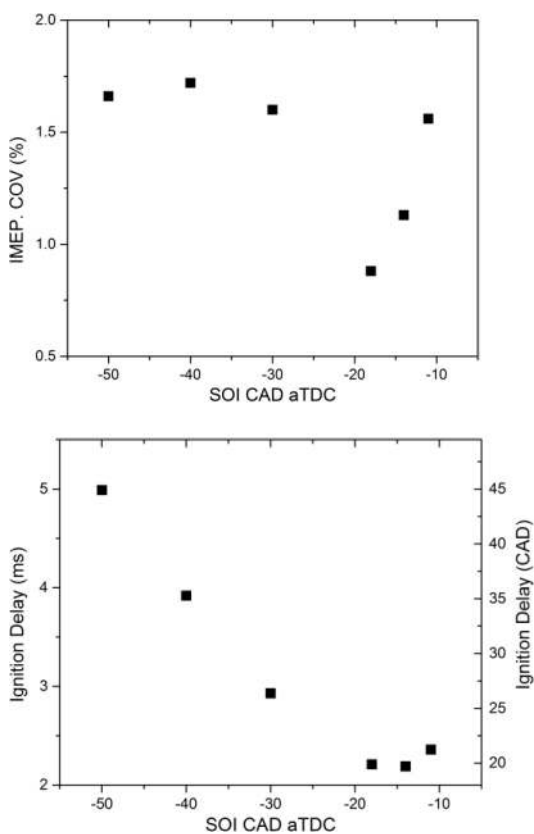
Figure 7. IMEP COV and ignition delay for the tested SOI.

Numerical Simulations Results

Motored Run

Full-cycle engine simulations were performed here. Simulations start before the exhaust valve opening (EVO) (160° crank angle (CA)) for a full cycle ending at 880° CA. A motored run is simulated first before moving to the GCI combusting cases. A motored run with a CR of 14 is simulated using the mesh described earlier and simulations ran from 160° CA to 880° CA. The experimental in-cylinder, intake port and exhaust port pressures are available for direct comparison. The earlier valve profiles are also utilized along with the measured intake temperature. The engine specifications and operating conditions for the CR 14 motored run are listed in Table 5. The default parameters and models in CONVERGE are adopted. This includes the RNG k-ε turbulent mixing model and the wall heat transfer model by O'Rourke and Amsden [49]. Originally, the

in-cylinder pressure at top dead center (TDC) is slightly over-predicted numerically when compared to experiments as can be seen from the blue curve in Figure 8. This difference is a combination of multiple factors such as the geometrical CR, the wall (piston, head, liner, intake and exhaust ports) temperatures are not certain and most importantly, the blow-by effect is not accounted for numerically. These uncertainties are accounted for by changing the effective CR in the simulations. The motored pressure trace can be matched by changing the effective CR to 13.85 as can be seen from the red dashed line in Figure 8.

Table 5. Engine specifications and modeling operating conditions for the CR 14 motored run.

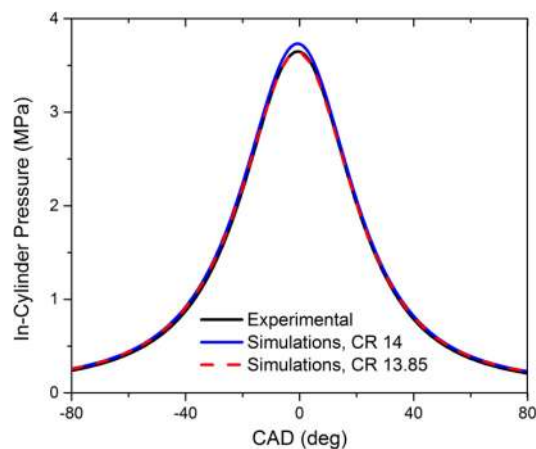| Geometric CR	14:1
Revolution per minute (RPM)	1500
EVO (`aTDC)	161
Intake temperature (K)	302.7

Figure 8. Experimental and calculated (changing the CR) in-cylinder pressure for the CR 14 motored run

GCI Cases

A GCI engine case is set up in CONVERGE using the same engine geometry. Straight-run Saudi Aramco light naphtha is used during the experiments [11, 26]. The same piezo electric outwardly opening hollow cone injector is used here and is simulated with the previously mentioned spray setup. The injection pressure is 130 bar, the fuel temperature is set to 363 K and the injected fuel is around 10 mg/cycle. The start of injection (SOI) is varied from -50 to -11 CAD aTDC. The engine speed is 1500 RPM and the same valve profiles of the motored runs are utilized. Few simulation parameters are listed in Table 6 where liner, head and piston temperatures are set to 463 K, 463 and 473 K respectively.

The surrogate formulation is very important in engine simulations. Because of the lack of reliable reduced chemical kinetic mechanisms for many relevant species, a primary reference fuel (PRF) or toluene primary reference fuel (TPRF) has to be used. The light naphtha has a sensitivity of 5 and hence a TPRF surrogate is developed here to match both the RON and MON of the actual fuel. The proportions of the toluene, n-heptane and iso-octane in the formulated surrogate are calculated using the blending rule by Kalghatgi et al. [50]. These proportions along with other properties of the TPRF surrogate and the light naphtha are presented in Table 7.

The droplet breakup and evaporation are also important factors for capturing the mixing and combustion correctly in the engine simulations. For the selected TPRF surrogate and light naphtha fuels, the temporal evolution of the heating and evaporation of a single droplet is calculated. For the light naphtha, the concentrations of all species identified in the detailed hydrocarbon analysis (DHA) were fed into the multi-component droplet heating and evaporation code. Figure 10 shows the predicted droplet surface temperature and radius of different fuel droplets with initial temperature of 300 K, initial radius of 10 μm and constant relative velocity of 10 m/s. The ambient air pressure and temperature are 0.3 MPa and 450 K, respectively. It is shown that the droplet lifetime of light naphtha is shorter than that of the TPRF surrogate. This is attributed to the high volatility of light naphtha compared to TPRF.. To properly capture the evaporative characteristics of the light naphtha, a 3 components surrogate containing n-pentane, n-hexane and 2,3-dimethyl-butane is formulated. The 3 components surrogate has mass fractions of 0.493, 0.266 and 0.241 for n-pentane, n-hexane and 2,3-dimethyl-butane, respectively. This 3 components surrogate has similar evaporative characteristics and physical properties to the light naphtha as can be seen from Figure 10 and Table 7. Subsequently, a new liquid properties file that is based on the 3 components surrogate is formulated and implemented in the model to be used for the TPRF chemical surrogate. In summary, the surrogate used in the engine simulations still has the TPRF68 as a chemical surrogate with the proportions listed in Table 7 but with the physical properties of the 3 components surrogate. Therefore, the TPRF68 surrogate is expected to have the same physical properties of the 3 components surrogate including the evaporative characteristics, density, heat of evaporation, conductivity, vapor pressure, heat capacity and surface tension. The methodology of formulating the chemical and physical surrogate of the light naphtha fuel for the engine CFD simulations is schematically presented in Figure 9. Finally, the latent heat of vaporization (LHV) of the TPRF68 surrogate is forced to be that of the light naphtha (44.9 MJ/kg) in all the subsequent simulations.

Table 6. GCI operating conditions for simulations.

Injector	hollow cone spray
SOI (aTDC)	-50 to -11
Injection pressure (bar)	130
Fuel temperature (K)	363
EGR level (%)	0
Start of simulations (°CA)	161
T_{liner} (K)	403
T_{head} (K)	403
T_{piston} (K)	423

Table 7. Properties of the tested surrogates along with the light naphtha.

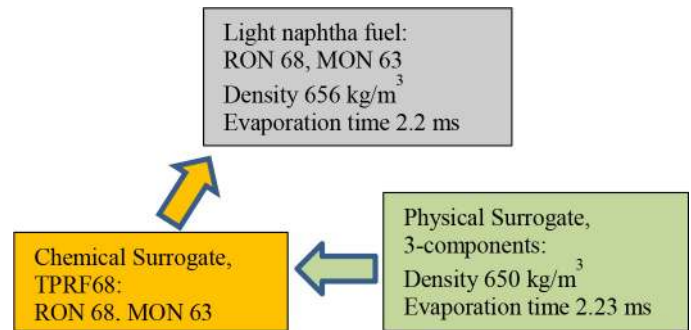| Fuel	Light naphtha	TPRF68	Physical Surrogate
Toluene mass fraction	-	0.3238	0.0
N-heptane mass fraction	-	0.3778	0.0
Iso-octane mass fraction	-	0.2984	0.0
n-pentane mass fraction	-	0.0	0.493
n-hexane mass fraction	-	0.0	0.266
2,3-dimethyl-butane mass fraction	-	0.0	0.241
RON	68	68	62.5
MON	63	63	60.0
Density at 293 K (kg/m^3)	656	695	650
H/C ratio	2.266	1.884	2.23

Figure 9. Methodology of formulating a surrogate for light naphtha for engine simulations.
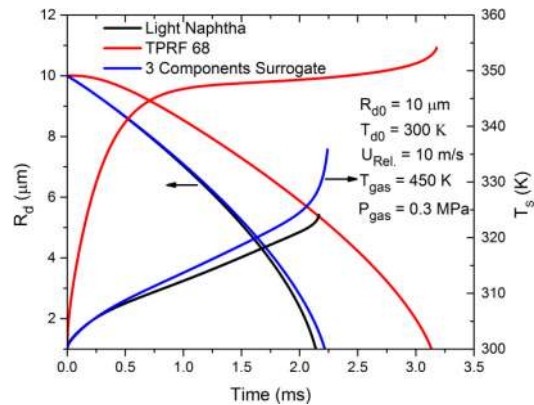

Figure 10. Plots of predicted droplet surface temperatures and radii versus time for different droplet mixtures.

A start of injection (SOI) sweep is performed here. Six different SOI of -50, -40, -30, -18, -14 and -11 CAD aTDC are simulated and compared with experiments. The injector used here has opening and closing ramps that have been estimated by Pischke et al. [51] to be 0.05 ms and 0.07 ms, respectively. The injector also has a 0.1 ms delay as observed experimentally [51]. The estimated mass flow rate is assumed to be of trapezoid shape starting at 0.1 ms after the SOI as previously implemented by Badra et al. [26]. The spray parameters for each case are presented in Table 8.The spray exit velocity is dependent on the in-cylinder pressure as shown in Eq. (1). For each SOI, the following steps are followed to setup the spray injection in CONVERGE:

1. The spray exit velocity is calculated using Eq. (1) where the chamber pressure is taken from the experimentally provided trace. Therefore, earlier injection such as -50 CAD aTDC has higher spray velocity because of the lower in-cylinder pressure during injection.

2. The average mass flow rate is calculated using the expression below,

$$\dot{m} = \text{injected mass} / \left(injection\ duration + \left(\frac{ramp\ up + ramp\ down}{2} \right) \right)$$

(5)

3. The imaginary nozzle diameter that is used in the spray exit velocity calculations in Converge using the KH-RT breakup model is then calculated by

$$d_0 = \sqrt{\frac{4\dot{m}}{\pi \rho U}}$$

(6)

4. The initial SMD is then calculated using Eq. (4).
5. The in-cylinder pressure increases during the injection process so the spray exit velocity should decrease accordingly (Eq. (1)). Therefore, the trapezoidal mass flow rate shape is altered in a way to reproduce the change in spray velocities for each of the different SOI.

The spray input and calculated parameters according to the steps detailed before are listed in Table 8 for the different SOI cases simulated here. The resulting spray exit velocities from the engine simulations for different SOI are presented in Figure 11. The start of injection is delayed by 0.1 ms which is reflected as 0.9 CAD at 1500 RPM. Earlier injection has higher spray exit velocities as can be observed from Figure 11 and the velocity slightly drops along the flat region because of the in-cylinder pressure increase during injection.

Table 8. Spray input and calculated parameters for the GCI simulations.

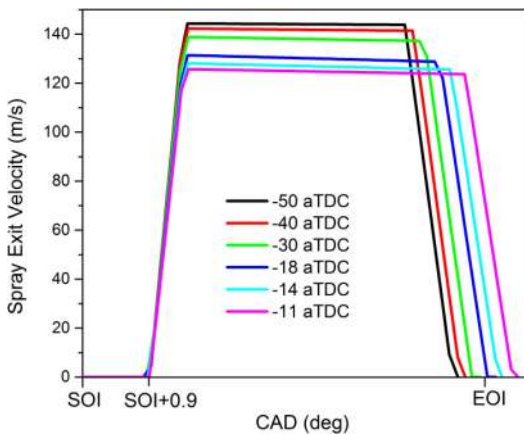| SOI (aTDC)	-50	-40	-30	-18	-14	-11
Injection duration (ms)	0.329	0.341	0.358	0.381	0.397	0.418
Injected mass (mg/cycle)	9.556	9.578	9.667	9.267	9.867	9
Spray exit velocity (m/s)	144.15	141.88	138.06	130.11	126.87	124.72
Mass flow rate $\dot{m}$ (g/s)	24.56	23.88	23.12	21.01	21.59	18.83
Calculated nozzle diameter (d_0) (mm)	0.617	0.613	0.611	0.6	0.616	0.58
Calculated SMD (D_0) (μm)	58.2	57.48	57.19	55.12	58.11	51.49

Figure 11. Spray exit velocities from the CFD engine simulations with different SOI.

The simulated in-cylinder pressure traces and heat release rates for the six GCI engine cases are presented in Figure 12. It is seen that the SOI of -30 CAD aTDC has the earliest combustion phasing followed by -40 CAD aTDC. SOI of -50 and -18 CAD aTDC have similar combustion phasing but rather different burn rates. It is clear that as the SOI is delayed further than-30 CAD aTDC, the combustion phasing is retarded more as can be seen from the -18, -14 and -11 CAD aTDC pressure and heat release curves presented in Figure 12. The simulated and measured CA10, 50 and 90 for these cases are shown in Figure 13. Figure 13 shows that the calculated CA10, 50 and 90 have minimums at -30 CAD aTDC and then start increasing

when moving either way away from -30 CAD aTDC. Experimentally, CA10 keeps decreasing for earlier injections (-50 and -40 CAD aTDC) and CA50 and 90 have minimums at -40 CAD aTDC. The experimental CAs are earlier than the calculated ones as can be observed from Figure 13. It is beyond the current scope of work to match the experimental combustion phasings but rather the observed trend with respect to different SOI. The burn rate, defined as CA90-CA10 is also presented in Figure 14 for the calculations and experiments. In agreement with the combustion phasing and CAs, the burn rate is fastest for SOI of -30 CAD aTDC. However, the experimental burn rates are faster than the calculated ones. This might be due to the differences in the CAs where earlier combustion phasing means faster burn because of the higher combustion pressures and temperatures.
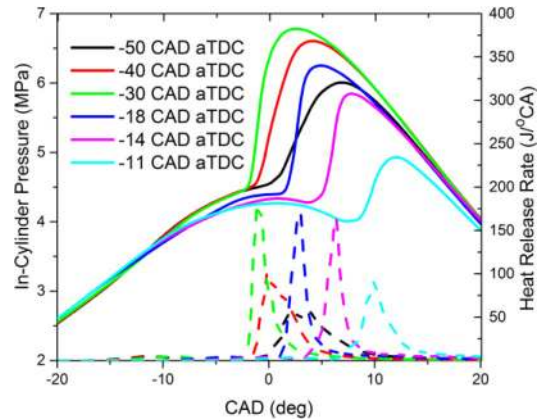

Figure 12. Simulated in-cylinder pressure (solid lines) and heat release rates (dashed lines)for the GCI engines cases with different SOI.
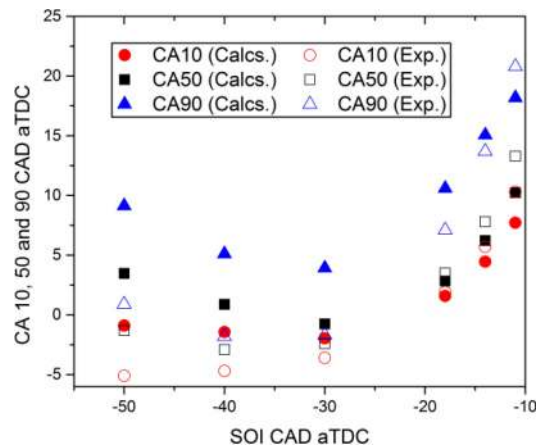

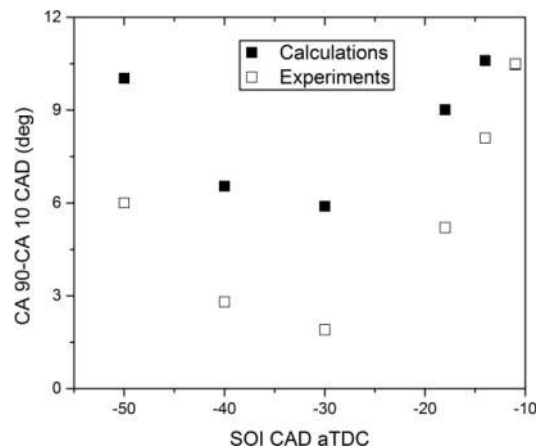Figure 13. CA10, 50 and 90 for the GCI engines cases with different SOI.

Figure 14. Burn rate (CA90-CA10) for the GCI engines cases with different SOI.
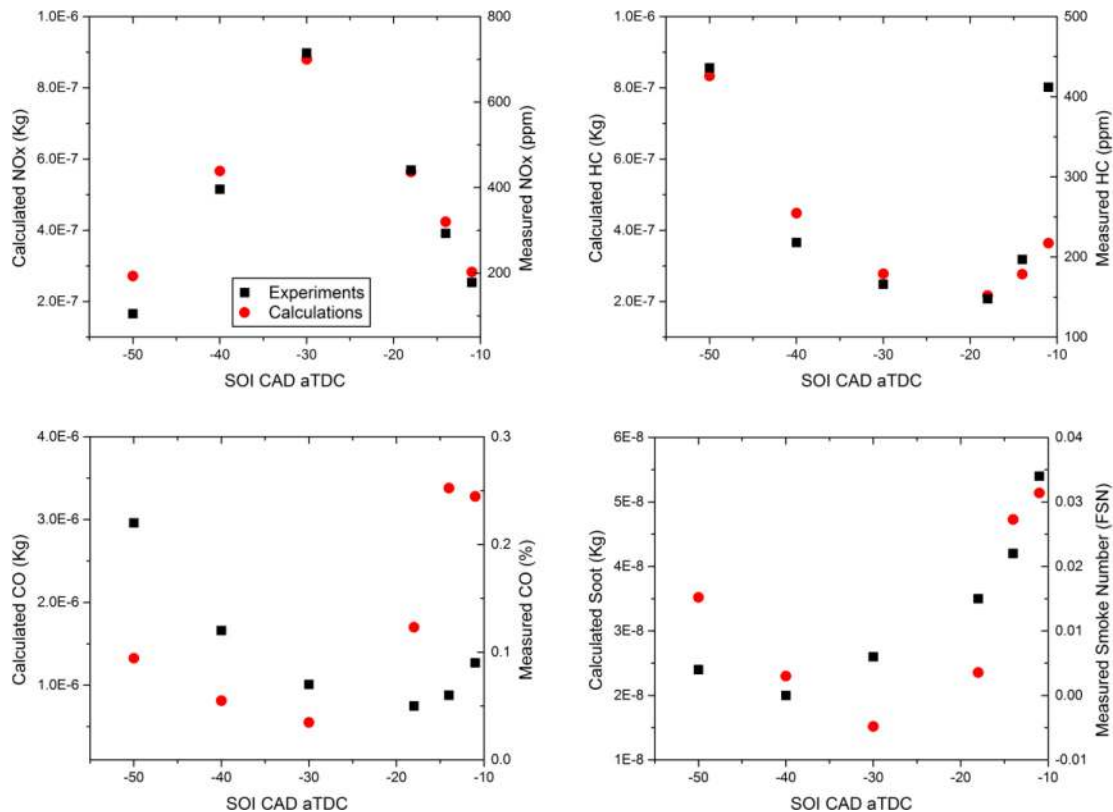
Figure 15. NOx, HC, CO and soot emissions for the GCI engines cases with different SOI.

The soot, NOx, HC and CO emissions from the simulations of the various GCI engine cases with different SOI are investigated here.

The values reported in the subsequent figures are taken from the simulations at 880 CAD (EVO), which is believed to be a representative CAD at the end of combustion; the trends remain consistent if emissions are taken at later CAD. The NOx, HC, CO and soot emissions from the simulations (kg) and experiments (ppm) are shown Figure 15. It is clearly seen in Figure 15 that the NOx emissions trends from the simulations and experiments are very similar where NOx peaks at SOI of -30 CAD aTDC and starts decreasing while advancing or retarding the SOI. This is due to the higher combustion temperatures at this particular SOI. The mean incylinder temperatures from the CFD simulations are presented in Figure 16 for the various tested cases. It is clear that NOx emissions are proportional to the in-cylinder mean temperatures. On the other hand, the HC emissions are lowest at -18 CAD aTDC from both the calculations and experiments. The experimental HC emissions at -11 CAD aTDC significantly increase as compared to the -14 CAD aTDC, whereas the simulations show slight increase for the same 2 SOIs This might be due to a deficiency in the utilized chemical model at rich equivalence ratios and/or a lack of accuracy in the turbulence model in control of mixing. The simulated soot and CO emissions are lowest at -30 CAD aTDC. The CO minimum value at SOI of -30 CAD aTDC is also because of the higher combustion temperatures which enable the CO to CO_2 conversion. However, the measured CO and smoke number show minimums at -18 and -40 CAD aTDC, respectively.
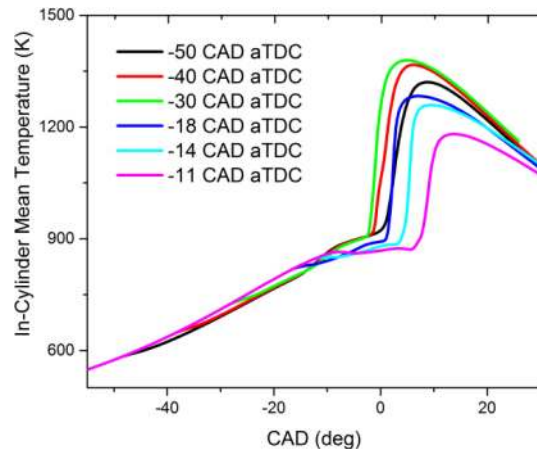

Figure 16. Simulated in-cylinder temperature for the GCI engines cases with different SOI.

An investigation of the fuel/air distribution within the in-cylinder region is performed here to explain the differences in combustion phasings observed at different SOI. Binned equivalence ratio (Φ)-temperature (T) maps for the various simulated cases is completed. The local equivalence ratio is calculated based on the fuel species and air (reactive equivalence ratio). The contours of Φ-T maps in the incylinder region for the different SOI cases are shown in Figure 17. These Φ-T maps are obtained from the non-reacting engine simulations at TDC (0 CAD) position and these are colored by the fuel mass fraction (toluene+n-heptane+iso-octane mass fractions). These iso-contours basically show at which equivalence ratios and temperatures all the injected fuel is located inside the combustion chamber. In addition, the mass-averaged equivalence ratios are presented in Figure 17 where these are calculated based on the expression below.
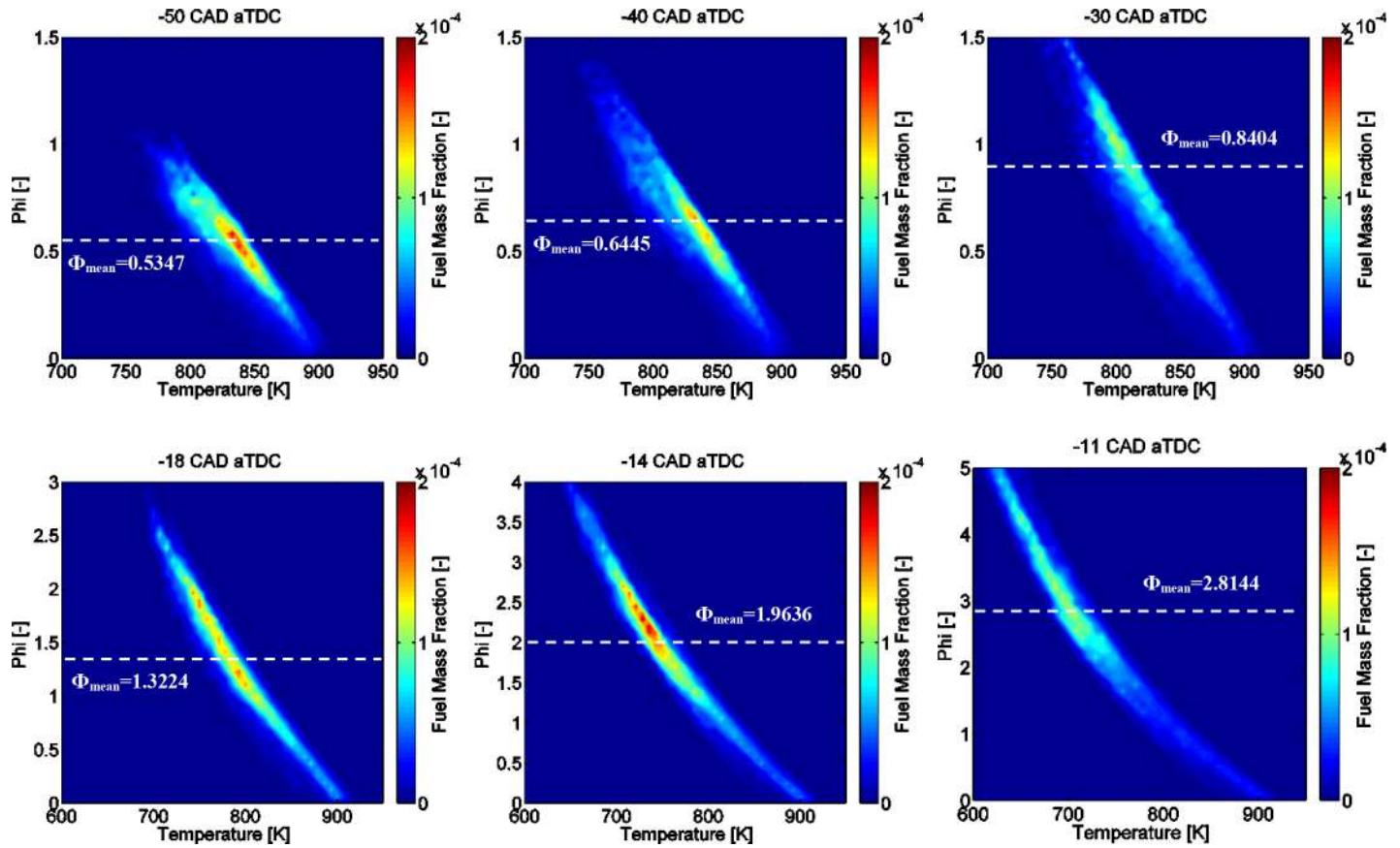
Figure 17. Non-reacting contours of Φ-T maps for the different GCI engine simulations with various SOI at TDC position.

$$\Phi_{mean} = \frac{\sum_{i=1}^{i=n} \Phi_i \times Fuel\ mass_i}{Total\ fuel\ mass\ injected\ per\ cycle}$$

(7)

where n is the total number of cells and i represents each cell in the in-cylinder domain. Figure 17 shows that most of the fuel is distributed around the equivalence ratio of 0.5 when injecting at -50 CAD aTDC. Similarly, the mass-averaged equivalence ratio for this particular condition is 0.5347 which indicates that the injected fuel did not mix perfectly well with all the in-cylinder air because the global equivalence ratios for these tested conditions are around 0.25. The distribution of the fuel changes when injecting at -40 CAD aTDC and most of fuel is located around 0.65 (Φ_{mean}=0.6445) equivalence ratio.. Most of the injected fuel in the domain is distributed at higher equivalence ratios as the SOI is retarded as can be seen from the Φ-T maps contours and mass-averaged equivalence ratios for SOI of -30, -18, -14 and -11 CAD aTDC. Most of the fuel is around stoichiometric equivalence ratios for SOI of -30 CAD aTDC and this distribution becomes much richer (around Φ=3) for SOI of - 11 CAD aTDC as can be observed from Figure 17. Note also that, when the distribution is leaner for earlier SOI (-50 CAD aTDC and - 40 CAD aTDC), the temperature is around 800 K-850 K. The temperature where the fuel is located decreases for later SOI (-14 and -11 CAD aTDC) to around 700 K. This is mainly due to the evaporative cooling of the fuel and the lower intake fuel temperature of 363 K as compared to the temperature of the in-cylinder compressed air (around 900 K).

Equivalence ratio contours at a cross plane through the middle of the injector are shown in Figure 18 for SOI of -50, -30 and -11 CAD aTDC at different CAD starting right after the SOI until TDC position from the non-reacting engine simulations. The contours for SOI of -50 CAD aTDC presented in Figure 18 show that the fuel spray is fully contained in the bowl from the start of injection up until the TDC position. The spray starts as symmetrical as can be seen from the contours at -45 CAD. The left side of the spray is pushed downwards by a vortex generated by the spray and also assisted by the air flow field due to the movement of the piston as can be seen from the contours at -40 CAD. The left side plume of the spray is fully contained by the piston bowl at -35 CAD and it remains the same for later CAD. The right side of the spray plume experiences a vortex that pushes it upwards as can be seen from the contours at -40 and -35 CAD. It actually approaches going in the squish region at -25 CAD. However, the air that is pushed out of the squish because of the piston motion forces the right side of the spray plume to change directions and hence being fully contained by the bowl as can be seen from the contours at -10 CAD and 0 CAD. Similarly, for SOI of -30 CAD aTDC, the spray is fully contained in the piston bowl due to similar sequence of events explained earlier for the -50 CAD aTDC SOI case. The left side of the spray is pushed downwards because of a developed vortex and it hits the piston bowl as can be observed from the -30 CAD aTDC SOI case at -20 CAD. The right side of the spray plume is pushed upwards and the flow coming out of the squish area keeps the entire injected fuel in the bowl region. Regarding SOI

of -11 CAD aTDC, the spray mainly dispenses in the area below the injector and is much richer than what was observed for -50 and -30 CAD aTDC SOI. A more detailed investigation of the fuel containment in the bowl is performed here. The mass-averaged equivalence ratio is calculated for both the in-cylinder and the bowl regions for three different SOI of -50, -30 and -11 CAD aTDC at various CAD timings. The mass-averaged equivalence ratio is calculated using Eq. (8). All the cells in the in-cylinder domain are considered when calculation the cylinder mass-averaged Φ. However, only the cells contained in a cylinder that has the same diameter of the bowl are considered when determining the bowl mass-averaged Φ. The results are shown in Figure 19, were it is found that the in-cylinder and bowl Φ_{mean} are very similar for all SOI at the different CAD up until 10 CAD. This indicates that all the fuel is contained in the bowl even for the earliest injection timing of -50 CAD aTDC. Slight differences are observed at CAD of 20 because the fuel starts being sucked back into the squish due to the flow motion when the piston starts going down.
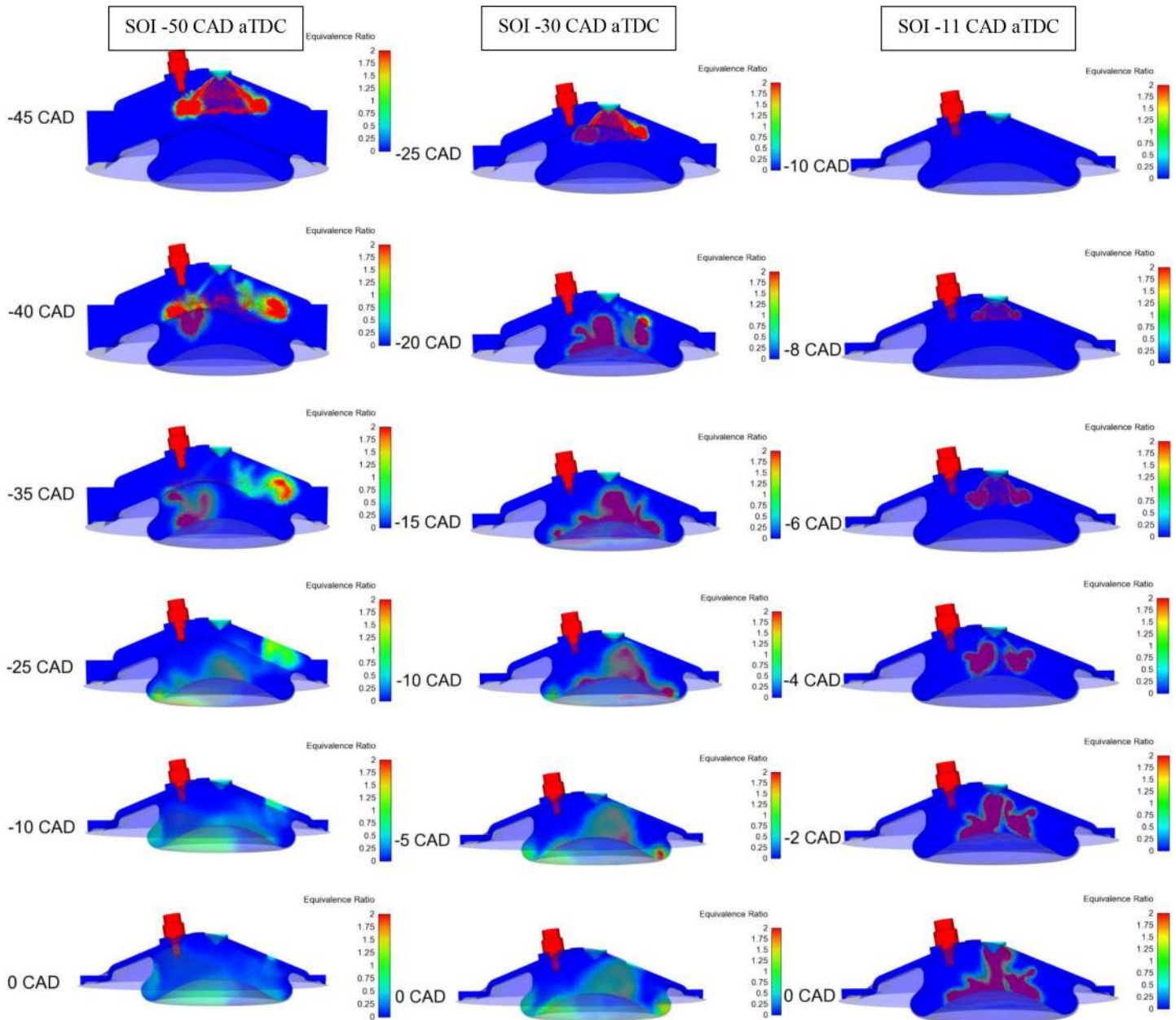

Figure 18. Equivalence ratio contours at a cross section through the middle of the injector for SOI of -50, -30 and -11 CAD aTDC at different timings.
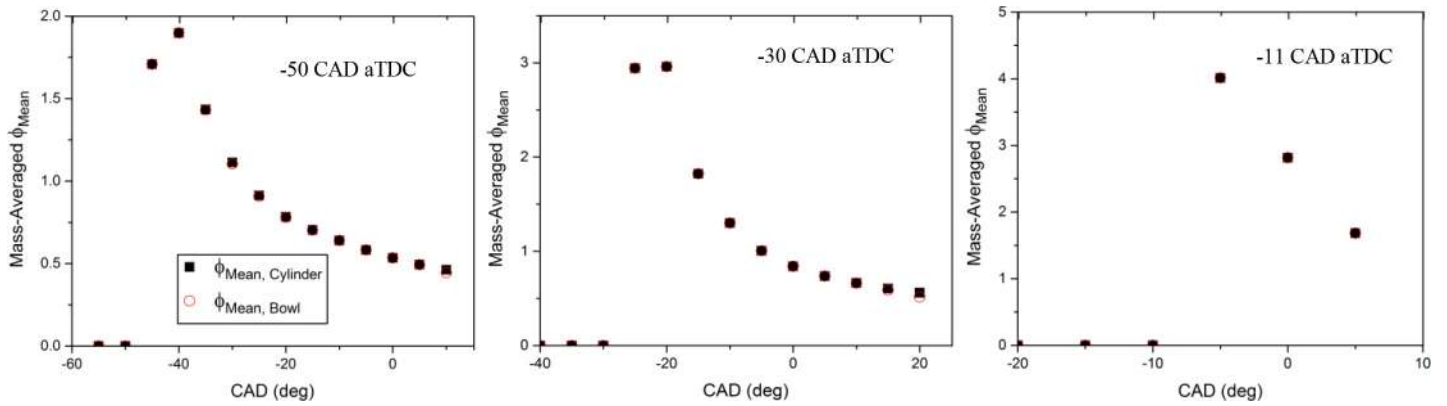
Figure 19. In-cylinder and bowl mass-averaged equivalence ratios for SOI of -50, -30 and -11 CAD aTDC for different CAD timings.
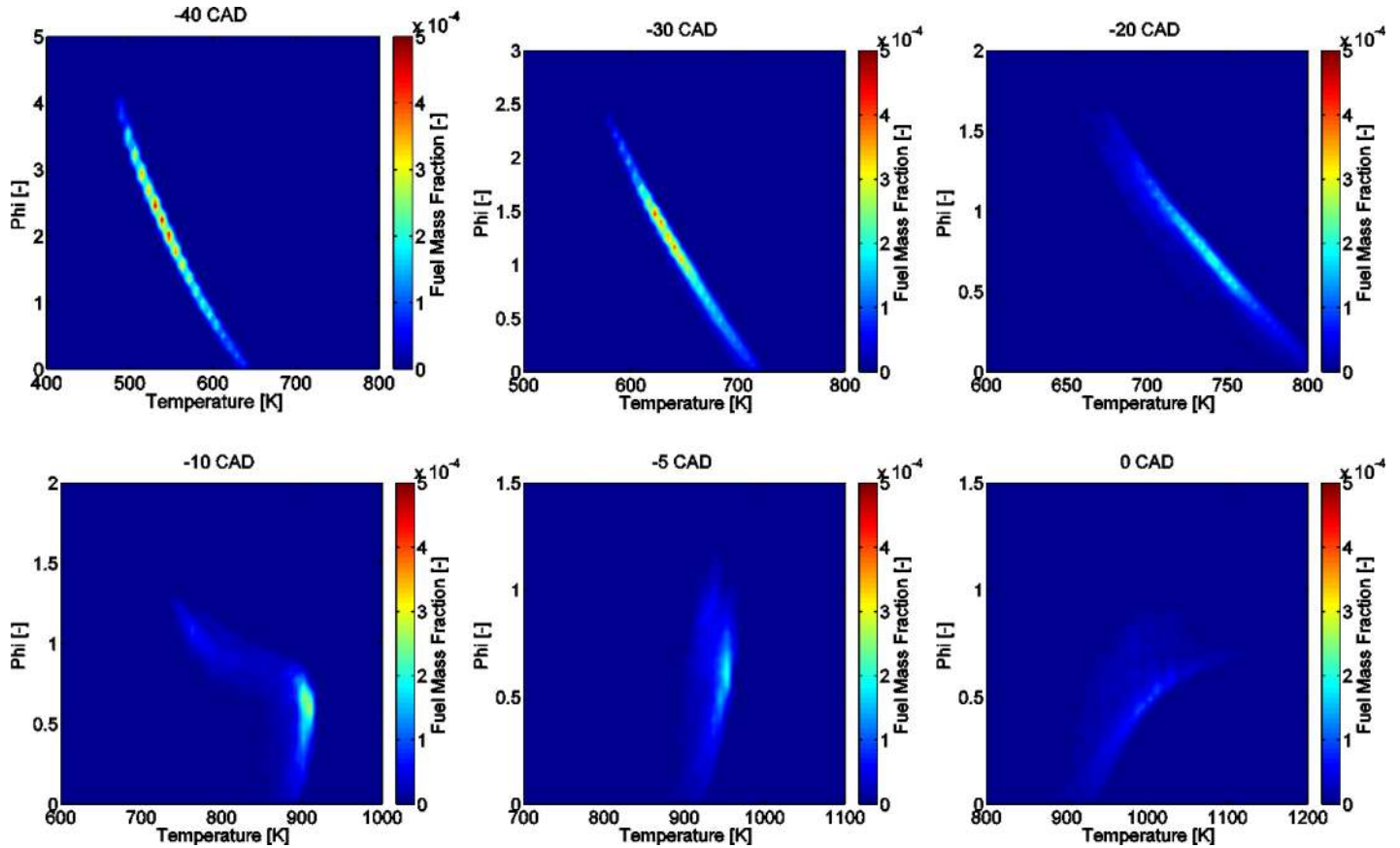

Figure 20. Contours of Φ-T maps from the reacting engine simulations with SOI of -50 CAD aTDC at different CAD.

The Φ-T maps contours from the reacting engine simulations are investigated here. The progress of Φ-T maps for the case with SOI of -50 CAD aTDC is presented in Figure 20. These contours are presented at -40, -30, -20, -10, -5 and 0 CAD. Most of the fuel is at very rich equivalence ratios at -40 CAD. This distribution becomes leaner at later CADs because of more time for mixing with the in-cylinder air. The fuel/air mixture goes through the low temperature heat release as can be seen from the contours at -10 CAD which is reflected as a small increase of the heat release rate curves shown in Figure 12. Ignition starts at equivalence ratios above 0.6 as can be observed from the Φ-T maps at 0 CAD.

The raw Φ-T maps for the reacting simulations with SOI of -50, -30 and -11 CAD aTDC are shown in Figure 21. These Φ-T maps are for each cell in the in-cylinder domain. Please note that the temperature x-axis is plotted on logarithmic scale to highlight the temperature increases at earlier CAD. The NOx and soot isles which were calculated at 50 bar [52] are also shown in Figure 21. The low temperature heat release is obvious from the black Φ-T maps at different timings for different SOI. Ignition starts at different equivalence ratios for different SOI. Ignition starts at Φ of 0.9 for SOI of -50 CAD aTDC. Regarding SOI of -30 CAD aTDC, ignition starts at slightly richer equivalence ratios (Φ around 1.5). However, ignition is initiated at very rich mixtures (Φ between 2.5 and 3) for SOI of -11

CAD aTDC. More cells have high combustion temperatures for SOI of -30 CAD aTDC because most of the fuel is distributed at equivalence ratios around stoichiometric which lead to higher adiabatic flame temperatures than leaner or richer combustion. This is consistent with the higher NOx and lower CO concentrations at this SOI as shown here. The soot is highest for SOI of -11 CAD aTDC as can be clearly seen from the more cells being in the soot isle.

To explain why the SOI of -30 CAD aTDC has the earliest combustion phasing, a simple analysis is performed. The constant volume homogenous ignition delay times for the TPRF fuel surrogate are calculated using the reduced mechanism [42] at different equivalence ratios with air ranging from 0.5 to 3, at different temperatures, and at a constant pressure of 40 bar which represents the condition at the start of ignition. The calculated ignition delay times are shown in Figure 22. It is found that the ignition delay times are shorter for richer TPRF68/air mixtures. For the subsequent analysis, the conditions for each SOI case are taken from the non-reacting Φ-T maps presented in Figure 17 at TDC position. In particular, the Φ-T conditions at the largest fuel concentration are selected. For SOI of -50 CAD aTDC, most (95%) of the fuel is at Φ = 0.45-0.6 and temperatures at 830-845 K. For SOI of -30 CAD aTDC, the conditions are shifted to Φ = 0.9-1.1 and T = 790-810 K, and for SOI of -11 CAD aTDC, Φ = 2.5-3.9 and T = 670 K-715 K. The homogeneous ignition delay times for these three different SOI cases are shown in Figure 22 as dotted lines. It is evident that the fuel Φ-T distribution for -30 CAD aTDC has the shortest ignition delay times as compared to the other two cases. The -50 CAD aTDC case has higher temperatures than the -30 CAD aTDC; however, the mixtures are leaner and hence they have longer ignition delay times. The opposite is true for the -11 CAD aTDC case, where the mixtures are much richer than the -30 CAD aTDC but they have lower temperatures, resulting in longer ignition delay times as can be seen from the black dotted line in Figure 22. This behavior is consistently reflected in the combustion phasing (CA10, CA50 and CA90) observed both experimentally and numerically for the SOI sweep.

The reasoning for this combustion phasing trend is more complicated than the constant volume homogeneous ignition delay times for the non-reacting Φ-T maps at TDC conditions. In the reacting simulations, low temperature heat releases are observed at -10 CAD for both the -50 and -30 CAD aTDC SOI, as seen from Figure 21. This will increase the temperature of the fuel/air mixtures to around 900 K-950 K. Subsequently, the entire mixture is awaiting ignition which takes place at -3 CAD and 0 CAD for SOI of -30 and -50 CAD aTDC, respectively. The combustion phasing for SOI of -30 CAD aTDC is shorter than -50 CAD aTDC even though the fuel/air mixture has less residence time to react and burn for the -30 Cad aTDC. This difference between the combustion phasings (3 CAD) of these two SOI cases can be explained by the different ignition delay time characteristics discussed earlier, where -30 CAD aTDC ignites at lower temperatures but richer mixtures. For SOI of -11 CAD aTDC, the mixtures starts going into low temperature heat release at around the TDC position (0 CAD) as can be seen from the black Φ-T map shown in Figure 21. Ignition starts at very rich equivalence ratios being around 3 after few CAD later (5 CAD). The delay in the startup of the low temperature heat release is partially due to the lower temperatures of the fuel containing cells as shown in Figure 17 and the black dotted line in Figure 22 and also due to the shorter residence time available for the fuel/air mixture to react.

The progress of the Φ-T map for the SOI of -50 CAD aTDC case presented in Figure 20 is shown (Figure 23) on the ignition delay time diagram for the same timings as in Figure 20. The fuel mixture is relatively cold at -40 CAD and hence has the longest ignition delay times. The mixture gets leaner and hotter as the CAD advances as can be seen from the -30 and -20 CAD. The mixture goes through the low temperature heat release at -10 CAD as evident from the larger temperature increase but it is still getting leaner because of the mixing. The temperature of the mixtures increases and its equivalence ratio decreases as compression is continued (-5 CAD). Finally, the main ignition occurs at 0 CAD where the temperatures are around 950 K and equivalence ratios of 0.6.
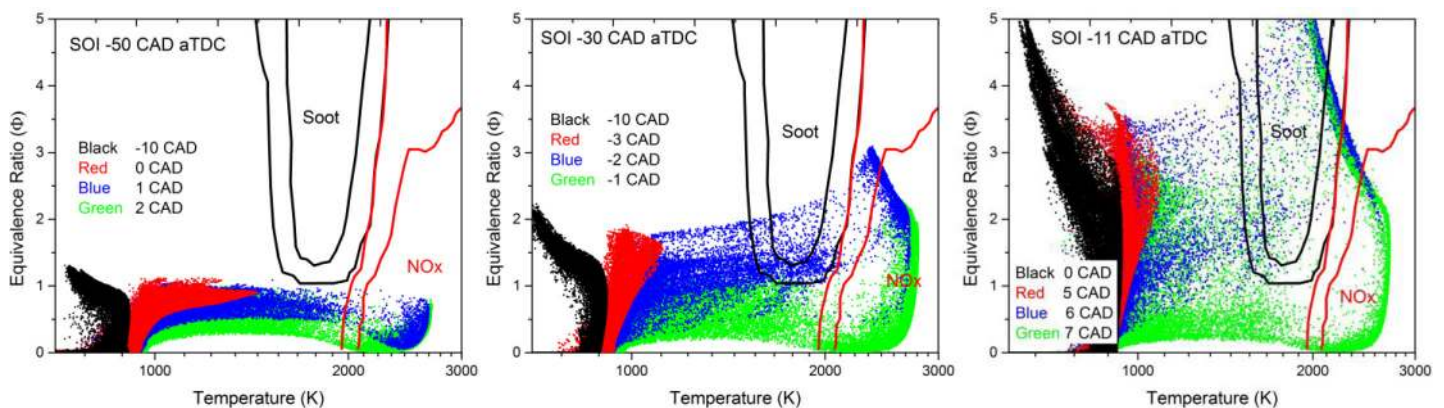

Figure 21. Reacting raw Φ-T maps for the simulated cases with SOI of -50, -30 and -11 CAD aTDC.
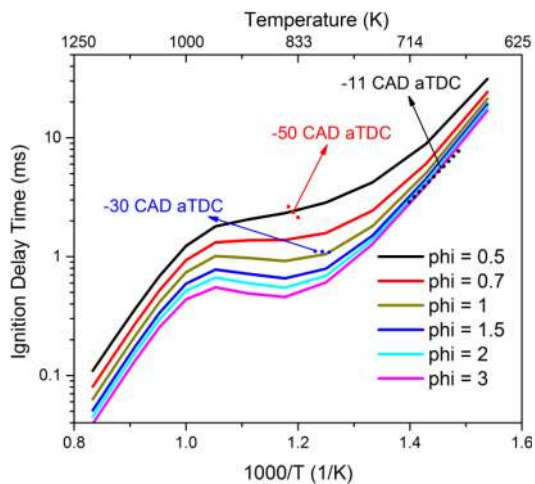
Figure 22. Calculated constant volume homogeneous ignition delay times for TPRF68/air mixtures at 40 bar.
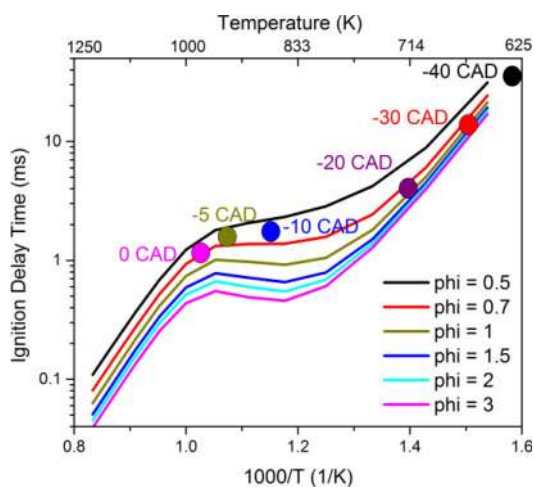

Figure 23. The ignition delay time progress for the reacting -50 CAD aTDC SOI case.

Summary/Conclusions

In this study, full-cycle high fidelity simulations of the Saudi Aramco GCI engines with naphtha fuels have been performed. We have investigated the effect of different injection timings (SOI) at part load conditions using light naphtha stream and one toluene primary reference fuel in a single cylinder engine under the GCI combustion mode both experimentally and numerically. The effect of fuel/air mixing on the combustion phasing of the engine was investigated in details using equivalence ratio-temperature maps and ignition delay times. Key findings are summarized as follows:

1. The measurements showed that an SOI of -40° CAD aTDC has the most advanced combustion phasing (CA50) and ignition is retarded for earlier and later SOI.
2. NOx emissions were highest for SOI of -30 CAD aTDC which corresponded to the lowest CO and HC emissions.
3. The experimental combustion phasing and emissions trends were fairly reproduced by the full-cycle CFD simulations.
4. The injected fuel was fully contained in the bowl even for the earliest SOI (-50 CAD aTDC).
5. The mass-averaged equivalence ratio increased while retarding the SOI.

6. The competition between the equivalence ratio and temperature is the controlling parameter in determining the combustion phasings.

This work is important to the GCI engine community because it details the ignition controlling parameters and presents some ideas to help designing the engines such as the higher sensitivity of CA50 at later SOI with higher combustion stability. This work also enables further extension to investigate the fuel's physical and chemical parameters on the combustion in GCI engines which is very important to design the future fuel for such engine technology.

References

1. U.S. Energy Information Administration. *International energy outlook 2013*, in, 2013.

2. ExxonMobil. *2012 Energy Outlook*, in, 2012.

3. Kalghatgi, G., "Fuel/Engine Interactions," (Warrendale, SAE International, 2013), doi:10.4271/R-409.

4. Kalghatgi, G. T., "The outlook for fuels for internal combustion engines", Int. J. Engine Res., 2014, doi:10.1177/1468087414526189.

5. Manente, V., Johansson, B.and Cannella, W., "Gasoline partially premixed combustion, the future of internal combustion engines?", Int. J. Engine Res., 12(3), 194-208, 2011.

6. Manente, V., Johansson, B., and Tunestal, P., "Partially Premixed Combustion at High Load using Gasoline and Ethanol, a Comparison with Diesel," SAE Technical Paper 2009-01-0944, 2009, doi:10.4271/2009-01-0944.

7. Manente, V., Johansson, B.and Tunestal, P., "Characterization of Partially Premixed Combustion With Ethanol: EGR Sweeps, Low and Maximum Loads", J. Eng. Gas. Turbines Power, 132(8), pp. 082802-082801-082807, 2010.

8. Manente, V., Zander, C., Johansson, B., Tunestal, P. et al., "An Advanced Internal Combustion Engine Concept for Low Emissions and High Efficiency from Idle to Max Load Using Gasoline Partially Premixed Combustion," SAE Technical Paper 2010-01-2198, 2010, doi:10.4271/2010-01-2198.

9. Chang, J., Kalghatgi, G., Amer, A., and Viollet, Y., "Enabling High Efficiency Direct Injection Engine with Naphtha Fuel through Partially Premixed Charge Compression Ignition Combustion," SAE Technical Paper 2012-01-0677, 2012, doi:10.4271/2012-01-0677.

10. Chang, J., Viollet, Y., Amer, A., and Kalghatgi, G., "Fuel Economy Potential of Partially Premixed Compression Ignition (PPCI) Combustion with Naphtha Fuel," SAE Technical Paper 2013-01-2701, 2013, doi:10.4271/2013-01-2701.

11. Viollet, Y., Chang, J., and Kalghatgi, G., "Compression Ratio and Derived Cetane Number Effects on Gasoline Compression Ignition Engine Running with Naphtha Fuels," *SAE Int. J. Fuels Lubr.* 7(2):412-426, 2014, doi:10.4271/2014-01-1301.

12. Borgqvist, P., Andersson, Ö., Tunestal, P.and Johansson, B., "The Low Load Limit of Gasoline Partially Premixed Combustion Using Negative Valve Overlap", J. Eng. Gas. Turbines Power, 135(6), pp. 062002-062001-062007, 2012.

13. Hanson, R., Splitter, D., and Reitz, R., "Operating a Heavy-Duty Direct-Injection Compression-Ignition Engine with Gasoline for Low Emissions," SAE Technical Paper 2009-01-1442, 2009, doi:10.4271/2009-01-1442.

14. Das Adhikary, B., Ra, Y., Reitz, R., and Ciatti, S., "Numerical Optimization of a Light-Duty Compression Ignition Engine Fuelled With Low-Octane Gasoline," SAE Technical Paper 2012-01-1336, 2012, doi:10.4271/2012-01-1336.

15. Ra, Y., Loeper, P., Andrie, M., Krieger, R. et al., "Gasoline DICI Engine Operation in the LTC Regime Using Triple-Pulse Injection," SAE Int. J. Engines 5(3):1109-1132, 2012, doi:10.4271/2012-01-1131.

16. Ciatti, S., Johnson, M., Das Adhikary, B., Reitz, R. et al., "Efficiency and Emissions performance of Multizone Stratified Compression Ignition Using Different Octane Fuels," SAE Technical Paper 2013-01-0263, 2013, doi:10.4271/2013-01-0263.

17. Solsjö, R., Jangi, M., Tuner, M., and Bai, X., "Large Eddy Simulation of Partially Premixed Combustion in an Internal Combustion Engine," SAE Technical Paper 2012-01-0139, 2012, doi:10.4271/2012-01-0139.

18. Kodavasal, J., Kolodziej, C. P., Ciatti, S.and Som, S., "Computational Fluid Dynamics Simulation of Gasoline Compression Ignition", Journal of Energy Resources Technology, 137(3), pp. 032212-032211-032213, 2015.

19. Onishi, S., Jo, S., Shoda, K., Jo, P. et al., "Active Thermo-Atmosphere Combustion (ATAC) - A New Combustion Process for Internal Combustion Engines," SAE Technical Paper 790501, 1979, doi:10.4271/790501.

20. Noguchi, M., Tanaka, Y., Tanaka, T., and Takeuchi, Y., "A Study on Gasoline Engine Combustion by Observation of Intermediate Reactive Products during Combustion," SAE Technical Paper 790840, 1979, doi:10.4271/790840.

21. Najt, P. and Foster, D., "Compression-Ignited Homogeneous Charge Combustion," SAE Technical Paper 830264, 1983, doi:10.4271/830264.

22. Thring, R., "Homogeneous-Charge Compression-Ignition (HCCI) Engines," SAE Technical Paper 892068, 1989, doi:10.4271/892068.

23. Iwabuchi, Y., Kawai, K., Shoji, T., and Takeda, Y., "Trial of New Concept Diesel Combustion System - Premixed Compression-Ignited Combustion -," SAE Technical Paper 1999-01-0185, 1999, doi:10.4271/1999-01-0185.

24. Kimura, S., Aoki, O., Ogawa, H., Muranaka, S. et al., "New Combustion Concept for Ultra-Clean and High-Efficiency Small DI Diesel Engines," SAE Technical Paper 1999-01-3681, 1999, doi:10.4271/1999-01-3681.

25. Ra, Y., Yun, J. E.and Reitz, R. D., "Numerical Parametric Study of Diesel Engine Operation with Gasoline", Combust. Sci. Technol., 181(2), 350-378, 2009, 10.1080/00102200802504665.

26. Badra, J. A., Sim, J., Elwardany, A., Jaasim, M.. et al., "Numerical Simulations of Hollow Cone Injection and Gasoline Compression Ignition Combustion with Naphtha Fuels", Journal of Energy Resources Technology, In press, JERT-16-1011, 2016.

27. Lefebvre, A. H., Gas Turbine Combustion, 2nd edition ed., CRC Press, 1983.

28. Williams, F. A., Combustion Theory, 2nd edition ed., Perseus Books, Reading Massachusetts, 1985.

29. Senecal, P. K., Schmidt, D. P., Nouar, I., Rutland, C. J., et al., "Modeling high-speed viscous liquid sheet atomization", Int. J. Multiphase Flow, 25(6-7), 1073-1097, 1999.

30. Schwarz, C., Schünemann, E., Durst, B., Fischer, J. et al., "Potentials of the Spray-Guided BMW DI Combustion System," SAE Technical Paper 2006-01-1265, 2006, doi:10.4271/2006-01-1265.

31. Senecal, P., Richards, K.and Pomraning, E., "CONVERGE (Version 2.2.0) Manual", Convergent Science Inc., Madison, WI (2014), 2014.

32. Senecal, P. K., Pomraning, E., Richards, K. J., Briggs, T. E.. et al., "Multi-Dimensional Modeling of Direct-Injection Diesel Spray Liquid Length and Flame Lift-off Length using CFD and Parallel Detailed Chemistry", SAE Technical Paper 2003-01-1043, 2003, doi:10.4271/2003-01-1043.

33. Heywood, J. B., Internal Combustion Engine Fundamentals, McGraw-Hill, 1988.

34. Hiroyasu, H. and Kadota, T., "Models for Combustion and Formation of Nitric Oxide and Soot in Direct Injection Diesel Engines," SAE Technical Paper 760129, 1976, doi:10.4271/760129.

35. Martin, D., Cardenas, M., Pischke, P.and Kneer, R., "Experimental investigation of near nozzle spray structure and velocity for a GDI hollow cone spray", Atomization Sprays, 20(12), 1065-1076, 2010.

36. Han, Z., Parrish, S., Farrell, P. V.and Reitz, R. D., "Modeling atomization processes of pressure-swirl hollow-cone fuel sprays", Atomization Sprays, 7(6), 663-684, 1997.

37. Schmidt, D., Nouar, I., Senecal, P., Rutland, C. et al., "Pressure-Swirl Atomization in the Near Field," SAE Technical Paper 1999-01-0496, 1999, doi:10.4271/1999-01-0496.

38. O'Rourke, P. J., Collective drop effects on vaporizing liquid sprays, in, Princeton University, 1981.

39. Schmidt, DP.and Rutland, C. J., "A New Droplet Collision Algorithm", Journal of Computational Physics, 164(1), 62-80, 2000.

40. Post, SL.and Abraham, J., "Modeling the outcome of drop-drop collisions in Diesel sprays", Int. J. Multiphase Flow, 28(6), 997-1019, 2002.

41. Amsden, A. A., O'Rourke, P. J.and Butler, T. D., Los Alamos National Laboratory, in, 1989, pp. Report No. LA-11560-MS.

42. Liu, Y.-D., Jia, M., Xie, M.-Z.and Pang, B., "Development of a New Skeletal Chemical Kinetic Model of Toluene Reference Fuel with Application to Gasoline Surrogate Fuels for Computational Fluid Dynamics Engine Simulation", Energy Fuels, 27(8), 4899-4909, 2013, 10.1021/ef4009955.

43. Sazhin, S., Droplets and Sprays, Springer, London, 2014.

44. Gusev, I. G., Krutitskii, P. A., Sazhin, S. S.and Elwardany, A. E., "New solutions to the species diffusion equation inside droplets in the presence of the moving boundary", Int. J. Heat Mass Transfer, 55(7-8), 2014-2021, 2012.

45. Sazhin, S. S., Elwardany, A., Krutitskii, P. A., Castanet, G., et al., "A simplified model for bi-component droplet heating and evaporation", Int. J. Heat Mass Transfer, 53(21-22), 4495-4505, 2010.

46. Sazhin, S. S., Al Qubeissi, M., Kolodnytska, R., Elwardany, A. E., et al., "Modelling of biodiesel fuel droplet heating and evaporation", Fuel, 115(0), 559-572, 2014.

47. Sazhin, S. S., Al Qubeissi, M., Nasiri, R., Gun'ko, V. M., et al., "A multi-dimensional quasi-discrete model for the analysis of Diesel fuel droplet heating and evaporation", Fuel, 129(0), 238-266, 2014.

48. Sazhin, S. S., Elwardany, A. E., Sazhina, E. M.and Heikal, M. R., "A quasi-discrete model for heating and evaporation of complex multicomponent hydrocarbon fuel droplets", Int. J. Heat Mass Transfer, 54(19-20), 4325-4332, 2011.

49. Amsden, A. A., Los Alamos National Laboratory, in, 1997, pp. Report No. LA-13313-MS.

50. Kalghatgi, G., Babiker, H., and Badra, J., "A Simple Method to Predict Knock Using Toluene, N-Heptane and Iso-Octane Blends (TPRF) as Gasoline Surrogates," *SAE Int. J. Engines* 8(2):505-519, 2015, doi:10.4271/2015-01-0757.

51. Pischke, P., Martin, D.and Kneer, R., "Combined spray model for gasoline direct injection hollow-cone sprays", Atomization Sprays, 20(4), 345-364, 2010.

52. Bergman, M.and Golovitchev, V. I., On Transient Temperature vs. Equivalence Ratio Emission Maps in Conjunction with 3D CFD Free Piston Engine Modeling, in: International Multidimentional Engine Modeling User's Group Meeting at the SAE World Congress, Detroit, USA, 2007.

Contact Information

Jihad Badra, PhD
Fuel Technology Division, Research and Development Center, Saudi Aramco
Building2293/C9, Dhahran 31311, KSA
jihad.badra@aramco.com
Tel:+9660138763056
Mob: +966544636600

Acknowledgments

Definitions/Abbreviations

C_D - discharge coefficient

d - diameter

D - Sauter mean diameter (SMD)

k_v - velocity coefficient

$\dot{m}$ - mass flow rate

p - pressure

U - injection velocity

t - liquid sheet thickness

T - temperature

Greek Symbols

ρ - density

θ - half of spray angle

Φ - equivalence ratio

Subscripts

0 - initial condition

c - chamber

inj - injection

l - liquid

n - nozzle

Abbreviations

3D - three dimensional

AMR - adaptive mesh refinement

CAD - crank angle degree

CAS - combustion system analysis

CFD - computational fluid dynamics

CI - compression ignition

COV - coefficient of variation

CR - compression ratio

DCN - derived cetane number

ED - effective diffusivity

ECL - exhaust complete lift

EGR - exhaust gas recirculation

ETC - effective thermal conductivity

EVC - exhaust valve closure

EVO - exhaust valve opening

GCI - gasoline compression ignition

GDI - gasoline direct injection

GHG - greenhouse gas

HC - hydrocarbons

HCCI - homogeneous charge compression ignition

H/C - hydrogen to carbon

ICL - intake complete lift

IQT - ignition quality tester

IVC - intake valve closure

IVO - intake valve opening

IMEP - indicated mean effective pressure

KR-RT - Kelvin-Helmholtz and Rayleigh-Taylor

LHV - lower heating value

LISA - linear instability sheet atomization

LN - light naphtha

LTC - low temperature combustion

MON - motor octane number

NMEP - net mean effective pressure

NOx - nitric oxides

NTC - no-time-counter

OECD - organization for economic co-operation and development

ON - octane number

PMEP - pumping mean effective pressure

ppm - parts per million

PRF - primary reference fuel

RANS - Reynolds-averaged Navier-Stokes

RNG - Reynolds normalization group

RON - research octane number

RPM - revolution per minute

SMD - sauter mean diameter

SOI - start of injection

TDC - top dead center

TPRF - toluene primary reference fuel